Annals of Glaciology



Article

Cite this article: Smith M, Thomson J (2020). Pancake sea ice kinematics and dynamics using shipboard stereo video. *Annals of Glaciology* **61**(82), 1–11. https://doi.org/10.1017/aog.2019.35

Received: 29 May 2019
Revised: 16 October 2019
Accepted: 17 October 2019
First published online: 18 November 2019

Key words:
Sea ice; atmosphere/ice/ocean interactions; sea-ice dynamics; sea-ice modeling; ice/ocean interactions

Author for correspondence:
Madison Smith, E-mail: mmsmith@uw.edu

© The Author(s) 2019. This is an Open Access article, distributed under the terms of the Creative Commons Attribution-NonCommercial-ShareAlike licence (http://creativecommons.org/licenses/by-nc-sa/4.0/), which permits non-commercial re-use, distribution, and reproduction in any medium, provided the same Creative Commons licence is included and the original work is properly cited. The written permission of Cambridge University Press must be obtained for commercial re-use.

cambridge.org/aog

Pancake sea ice kinematics and dynamics using shipboard stereo video

Madison Smith and Jim Thomson

Applied Physics Laboratory, University of Washington, Seattle, WA, USA

Abstract

In the marginal ice zone, surface waves drive motion of sea ice floes. The motion of floes relative to each other can cause periodic collisions, and drives the formation of pancake sea ice. Additionally, the motion of floes relative to the water results in turbulence generation at the interface between the ice and ocean below. These are important processes for the formation and growth of pancakes, and likely contribute to wave energy loss. Models and laboratory studies have been used to describe these motions, but there have been no in situ observations of relative ice velocities in a natural wave field. Here, we use shipboard stereo video to measure wave motion and relative motion of pancake floes simultaneously. The relative velocities of pancake floes are typically small compared to wave orbital motion (i.e. floes mostly follow the wave orbits). We find that relative velocities are well-captured by existing phase-resolved models, and are only somewhat over-estimated by using bulk wave parameters. Under the conditions observed, estimates of wave energy loss from ice–ocean turbulence are much larger than from pancake collisions. Increased relative pancake floe velocities in steeper wave fields may then result in more wave attenuation by increasing ice–ocean shear.

Introduction

Pancake ice is a type of sea ice that is often found in areas where new ice formation is coincident with large surface waves. This ice type has been commonly observed in the Southern Ocean (Treshnikov, 1967; Lange and others, 1989) as well as the Arctic Ocean, but previously observations in the Arctic were limited to areas open to other oceans such as the Okhotsk Sea and Bering Sea. Observations of pancake ice in the Central Arctic basin have become more commonplace with seasonal sea ice retreat in recent years (Thomson and others, 2018). Pancake ice has also been observed in large bodies of freshwater, including a number of northern lakes and rivers (e.g., Rumer and others, 1979; Campbell and others, 2014).

Conceptually, pancake ice formation and growth can be divided into three sequential stages: the formation of a grease or frazil ice layer, formation and growth of pancake floes, and the formation of composite pancakes by welding together of individual floes (Shen and others, 2001). Both the growth and welding of pancake floes depend strongly on the presence of dynamic wave motion. The gradient of wave orbital velocities across each wave drives relative motion of floes towards (and away from) each other (Fig. 1). This motion can result in the floe–floe collisions that are critical to pancake formation and subsequent growth. Doble and others (2003) and Doble (2009) found that growth due to collisions is primarily a result of the 'scavenging' of frazil ice from the water onto the tops of pancake floes. Doble (2009) suggested that scavenging occurs because of the reduction in frazil area as floes converge with wave motion.

There has been substantial observational and theoretical progress to understand the transformation of waves propagating into sea ice (Shen, 2019). Although many mechanisms have been proposed and examined to account for the attenuation of wave energy in sea ice, it is still not clear which mechanisms dominate (Squire, 2019). Part of the challenge is that the dynamics are sensitive to ice type. The collisions of sea ice floes are one proposed mechanism that can dissipate wave energy (Shen and Squire, 1998). This may be relatively important in pancake sea ice, where the energy associated with the impact is observed to accelerate the ice growth. Another proposed mechanism for energy dissipation is the generation of turbulence by shear between the rough ice and the ocean below (Kohout and others, 2011). Quantification of each proposed attenuation mechanism based on wave and ice conditions is needed for accurate prediction of wave conditions throughout sea ice-covered areas. The field observations for such quantification are rare, but efforts to model floe motion due to waves have advanced our understanding of these processes.

Prior work to describe ice floe motion in periodic wave fields has utilized simple physical models to predict the kinematics and dynamics. The simplest model that can be thought of is that ice will simply follow wave orbital velocities (Fig. 1). A 2D model of a sea ice field was able to produce physically reasonable results of floe motion and collisions by simply assuming that floes follow orbital motions at the free surface (Rottier, 1992). Many models for sea ice motion have been based on the slope-sliding model (Rumer and others, 1979) in which there is an additional force on floes as a result of gravity pulling them down the sloped surface of each wave (Grotmaack and Meylan, 2006). This theory has been utilized to describe expected frequency and magnitude of floe collisions (e.g., Shen and Ackley, 1991) and the associated

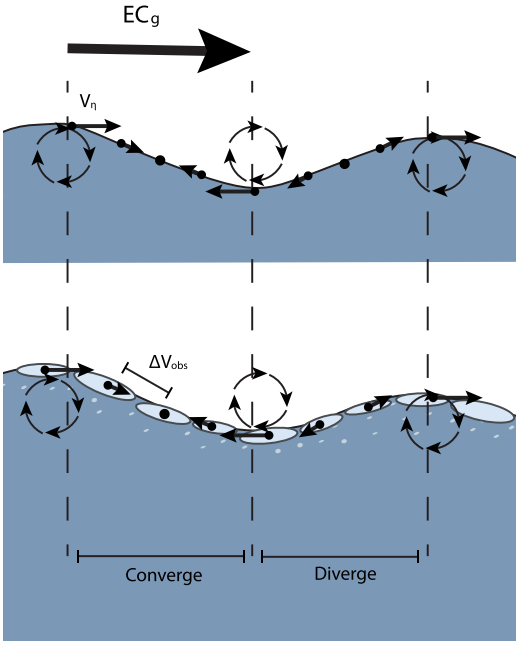


Fig. 1. Schematic of motion induced by wave orbital motion at the ocean surface without sea ice (top) and with sea ice (bottom). The gradient in the orbital velocity (V_η) results in relative velocity of ice floes (ΔV_{obs}), which causes floes to converge on the front face of the wave and diverge on the back face of the wave. The direction of wave energy flux (EC_g) in this schematic is from left to right.

attenuation of wave energy (Shen and Squire, 1998). Another model using linear-potential flow theory has been suggested to be applicable where floe diameters are approximately equal to or greater than the wavelength (Meylan and others, 2015).

Recent work has developed a numerical model for ice floe motion (Herman, 2011, 2013). This model framework was adapted in Herman (2018) to describe surge motions, similar to those predicted by the slope-sliding model, and the resulting collisions. A crucial difference between the model by Herman (2018) and prior models is the method for computing the forces. While previous models assumed that the floes are infinitely small and forces were computed at the center of mass, the Herman model integrates forces over the surface of each floe.

A number of laboratory studies in recent years have examined the accuracy of models and theory describing ice floe motion and collisions. Experiments testing the response of a single floe to a wave field have found that floe motion can largely be predicted by simple models when the radius is small compared to the wavelength (e.g., Meylan and others, 2015; Yiew and others, 2016). Investigations of collisions have mostly used two floating disks representing ice floes to show that collisions can similarly be predicted by these simple models for floe motion (e.g., Yiew and others, 2017; Li and others, 2018). There have, to our knowledge, not been any phase-resolved field observations of floe motion within natural sea ice or realistic wave fields (i.e., directional and irregular seas). The lack of measurements of pancake sea ice motion in the field stems largely from the difficulty of measuring them. Not only are ice-covered areas with substantial surface waves challenging to work in, but capturing lateral ice motion requires both spatial and temporal coverage.

Stereo camera systems have been gaining popularity as a method for measuring three-dimensional ocean wave fields from both stationary and mobile platforms. A number of recent studies have demonstrated the utility of this method in capturing phase-resolved wave processes, such as wave slope and breaking (Schwendeman and Thomson, 2017; Benetazzo and others, 2017). Additionally, shipboard stereo cameras are useful for measuring the properties of ice-covered areas. Prior studies utilized stereo cameras to provide consistent and continuous estimates of sea ice characteristics, including thickness, texture and floe size distribution (Rohith and others, 2009; Niioka and Kohei, 2010; Alberello and others, 2019). To our knowledge, only one study has utilized stereo imagery to capture waves in ice (Campbell and others, 2014). That study used a shore-based stereo imaging system on a lake to measure changes in wave spectra and energy flux through three different ice types. Their results indicated the potential of stereo systems for capturing the complex dynamics of waves in sea ice with both spatial and temporal characterization of the surface.

Here, a shipboard stereo video system is used to provide unique phase-resolved measurements of pancake sea ice floe velocities relative to each other. Measurements of relative velocities under a variety of wave conditions are compared to two models for pancake motion, with the goal of determining which model best describes in situ observations. We resolve the convergence (and collision) of ice floes on the front face of individual waves, as well as the divergence on the back face of waves. We determine a characteristic relative velocity of the ice floes for each set of conditions, and we relate these to bulk wave parameters. We then discuss the implications of the results for growth and development of pancake floes, and for wave energy loss in pancake ice. The relative velocity between floes is the primary variable controlling whether floes collide and the turbulence produced by their motion, so is thus applied as the key kinematic parameter for describing these dynamics.

Methods

Shipboard stereo camera setup

Measurements were made from shipboard stereo systems mounted on the rails of 04 deck of the R/V *Sikuliaq* during the 'Sea State and Boundary Layer Physics of the Emerging Arctic Ocean' experiment that took place on October–November 2015. All observations were made in newly formed ice in the Beaufort Sea marginal ice zone. A full map of the cruise track and description of conditions can be found in Thomson and others (2018).

Two stereo systems (Schwendeman and Thomson, 2017) were mounted on the starboard and port rails aft of the bridge, 16.5 m above mean sea level. Each system consists of two Point Grey Flea2 cameras separated by 2 m, as shown in Figure 2a. Each of these cameras has a 9-mm fixed focal length lens, giving an ~30° horizontal field of view, and was mounted with a look angle 18° below horizontal. The frame of view of these cameras begins ~40 m away from the ship, but varies over time with the rolling of the ship. The ship was oriented perpendicular to the direction of wave propagation during video collection in order to avoid wave reflection and interference. By qualitative inspection of the video recordings, there were no obvious wave reflections from the ship (see Supplemental Video). An additional Point Grey Flea2G camera with a 2.8-mm fixed focal length lens was mounted centered between the Flea2 cameras. This camera had a wider field of view in order to capture the horizon in most images and allow the calculation of pitch and roll following Schwendeman and Thomson (2015). All cameras recorded at 5 Hz.

A Novatel combined inertial motion unit (IMU) and global navigation satellite system (GNSS) were mounted with the cameras on the port side. The antennas can be seen in the photo in Figure 2a. This IMU system is used to measure the position of the cameras, as well as the pitch and roll of the ship.

This study utilizes observations made with the stereo system during five periods. Table 1 shows the date and starting time,

https://doi.org/10.1017/aog.2019.35 Published online by Cambridge University Press

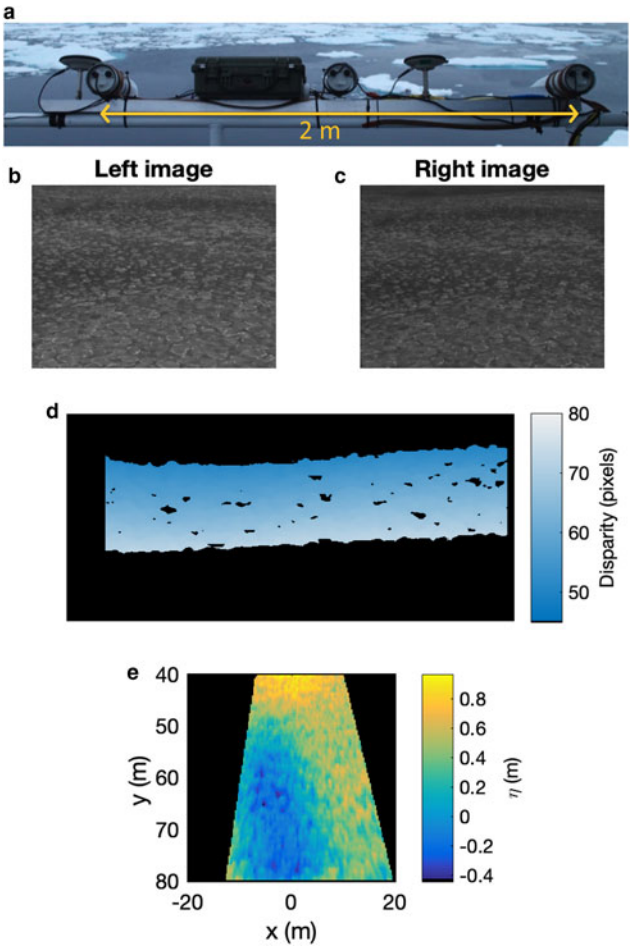


Fig. 2. Stereo setup and example of processing steps. Panel (a) shows the stereo setup on the port side rail of the *R/V Sikuliaq*, with IMU-GNSS antennas mounted alongside cameras for stereo retrieval. Subsequent images show (b,c) an example of a pair of rectified stereo images, (d) the corresponding disparity map (in pixels) and (e) the resulting surface elevation map.

and bulk wave and ice conditions for each. Stereo observations are collected in up to 30 min bursts, which are processed to determine bulk wave characteristics following the steps described in the next section. Approximately 135 s of each observation are processed to characterize floe motion.

Wave estimates from stereo video

The stereo images are processed to obtain wave results following the methods described in Schwendeman and Thomson (2017). The basic processing steps are calibration of the camera system, synchronization of all data streams, rectification of images and rotation to the Earth reference frame. The methods are summarized here, but additional details may be found in Schwendeman and Thomson (2017).

Calibrations for the stereo camera setup are produced using the built-in routine in the Matlab Computer Vision toolbox. Sets of images of a 5×10 black and white checkerboard with $4''$ squares were acquired after the cameras were mounted on the ship during mobilization, prior to data collection. The Matlab calibration routine utilizes these images to determine both intrinsic and extrinsic parameters of the stereo cameras.

The Novatel IMU data were separately recorded, and thus it is necessary to synchronize with images in post-processing. Offsets between the image and IMU data streams are determined using the cross-correlation of the time series of pitch derived from the horizon tracking method from Schwendeman and Thomson (2015) and that recorded by the Novatel. These offsets are used to align IMU pitch and roll with the images, as the IMU is more accurate than the horizon tracking method, particularly in low wave conditions.

Table 1. Summary of bulk wave and ice conditions for observations. Wave parameters are obtained by processing 5 min stereo video bursts, and ice observations are from both processing stereo images (radius, r) and shipboard visual observations (thickness, z)

Observation	H_s [m]	T_e [s]	L_e [m]	r [m]	z [cm]	$k \cdot r$ [-]
11 October 21:30	2.5	7.2	82	0.65	8	0.05
24 October 22:20	1.0	4.5	31	0.65	~20	0.13
24 October 23:18	0.9	4.6	34	0.52	5	0.10
01 November 19:17	1.0	4.3	29	0.51	6	0.11
01 November 19:35	1.1	4.8	37	0.58	7	0.10

Rectification is a transformation process to project images onto a common plane, and is necessary for identification of matching pixels. Rectification slightly warps the epipolar lines in each image to make them horizontal, such that it appears that the images are simply horizontally offset. Pixels from left images are then mapped onto the right images to create a disparity map, showing the difference in pixel location for the same geographic location at each point. This is done using the Semiglobal algorithm in the Matlab Computer Vision Toolbox. An example of a pair of images and the resulting disparity map is shown in Figures 2b–d.

The disparity map is rotated into the Earth reference frame in order to produce a surface elevation map in which waves can be observed. This is done using pitch and roll values from the synchronized IMU time series. Elevation map results are then interpolated onto a regular grid with 0.25 m spacing. An example map of surface elevations is shown in Figure 2e.

Wave spectra are calculated from the gridded elevation maps using the Fast Fourier Transform (FFT) of the time series of surface elevation at each point, with 75% overlap. This is equivalent to treating each grid cell as a virtual wave buoy. The resulting spectra are then averaged together (all grid points) for each 5 min burst of data analyzed. Bulk wave characteristics are determined from the spectra, including the significant wave height (H_s), peak wave period (T_p) and energy-weighted wave period (T_e). The energy-weighted wave period, defined as $T_e = \int E(f)\,\mathrm{d}f / \int fE(f)\,\mathrm{d}f$, is used to estimate average wavenumber k and wavelength L_e for use in subsequent calculations. Wavelength is calculated using $L_e = gT_e^2/2\pi$ as Collins and others (2018) did not find any indication of deviation from linear deep water dispersion in these ice types.

Comparison with wave buoys

Previous application of this stereo setup in open water by Schwendeman and Thomson (2017) showed good agreement with traditional measurements from wave buoys. Here, we validate the stereo performance in the presence of sea ice before proceeding with the analysis. Spectra from the stereo system in sea ice are compared with simultaneously deployed SWIFT wave buoys. SWIFT buoys capture the wave signal by measuring horizontal displacement with a GPS receiver in 8 min intervals, as described in further detail in Thomson (2012) and Smith and others (2018).

Figure 3 shows a comparison of wave spectra measured on 11 October 2015 21:30, where SWIFT 15 was within 2 km of the ship, and SWIFT 14 was ~20 km from the ship. The spectrum produced from the stereo video observations (black line) captures all the key features of the spectra from the wave buoys. There is a small amount of extra energy at the peak period as a result of uncorrected ship motion, which was observed in the open water comparison done by Schwendeman and Thomson (2017) as well, and additionally too much energy observed at frequencies

https://doi.org/10.1017/aog.2019.35 Published online by Cambridge University Press

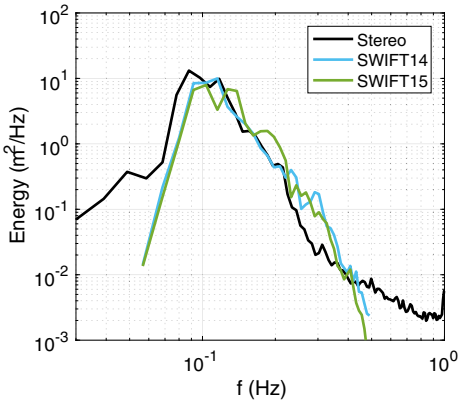


Fig. 3. Comparison of wave energy spectra as a function of frequency estimated from stereo video (black) two SWIFT wave buoys deployed nearby (blue and green). Observations are from 11 October 21:30.

below 0.06 Hz. There is clear noise contamination at high frequencies ($f > 0.4$ Hz), but those frequencies are beyond the scope of the present study. SWIFT deployments during other stereo observation periods were not as well collocated. Comparisons of spectra from these periods are provided as Supplementary material. Although features of the wave spectra differ between the SWIFT buoys and stereo observations due to variation in the ice conditions, the comparisons generally support the validation of stereo measurements across a range of wave conditions.

Wave orbital velocities

The velocity due to wave orbitals $\overline{V_\eta}$ is the underlying motion that ice floes move with, and relative to, with the passage of each wave (Fig. 1). An estimate of the phase-resolved wave orbital motion can be calculated by applying linear wave theory using the time series of surface elevation, η, as

$$\overline{V_\eta}(t) = \frac{2\pi}{T(t)}\eta. \tag{1}$$

Here, we use a time series of wave period T calculated from the η signal using the zero-crossing method with a smoothing interval of 2 s. This phase-resolved estimate represents an average of velocities over the gridded domain. The overline is used throughout to represent such spatial averages, and brackets represent temporal averages. We can use the definition of $\eta = (H_{\mathrm{rms}}/2)\cos(kx - \omega t)$ to estimate the time-average of the absolute orbital velocities as

$$\left\langle |\overline{V_\eta}| \right\rangle = \frac{2H_s}{T_e}. \tag{2}$$

Estimates of relative ice velocity

Observation of relative ice velocities

Estimates of relative sea ice velocities are made using a series of ortho-rectified images from one side of the stereo pair, recorded at 5 Hz. We use the left image, but the results are unaffected by the side chosen due to the overlapping footprint. An example of a single ortho-rectified image projected to geographic coordinates is shown in Figure 4, where the ship is located approximately at $y = 0$.

All estimates are made over a 8×25 m box centered in the domain, demonstrated by the blue rectangles in Figure 4. Some observations contained periods with substantial rolling, such that the footprint of the stereo camera system changed significantly over time. The size of the analysis box was chosen to balance the desire to minimize the effect of rolling (by using a smaller box) with the need to provide a robust estimate (by doing a large spatial average). When the rolling was substantial enough such that any part of the analysis box was not captured, those images were ignored in subsequent calculations. The aspect ratio of the box was chosen to have the smallest reasonable width. As the wave propagation direction was typically parallel to the ship (or, in the x-direction of Fig. 4) this isolates the phase of a wave propagating through the box. The chosen analysis box dimensions limit the observable wave period to a minimum of 2.3 s, with a width of 8 m in the primary direction of wave propagation for all observation periods.

Characteristic relative velocities of pancake floes ($\overline{\Delta V_{\mathrm{obs}}}$) are calculated from images using the change in average distance between floes. We are not able to determine floe motion directly, primarily due to the limited resolution of the system, which prevents tracking individual floes. The stereo reconstruction provides us with changes in surface elevation, and relative velocities are estimated using the raw images.

In order to calculate average distance between floes, we assume that the floes in each image have uniform radius and are evenly spaced, such that the areal concentration A can be estimated as

$$A = \frac{\frac{1}{2}\pi r^2}{l^2}, \tag{3}$$

where l is the length of the box formed by connecting the center of floes (shown schematically in Fig. 5). The average distance between floes is calculated as:

$$\overline{D_{\mathrm{obs}}}(t) = \sqrt{\frac{\pi(2\bar{r})^2}{4A(t)}} - 2\bar{r}, \tag{4}$$

where $\bar{r}$ is the floe radius, and overbars indicate spatial averages (Fig. 5). Estimation of $\bar{r}$ and A to determine $\overline{D_{\mathrm{obs}}}$ from observations is described below and demonstrated in Figure 6.

Floe radius is determined from the equivalent diameter of objects in thresholded images, produced using an adaptive threshold from the Matlab image processing toolbox. The right panel of Figure 4 shows an example thresholded image, where each white object is considered an individual floe. An average $\bar{r}$ is calculated for each frame. A linear fit to the time series of $\bar{r}$ is used to avoid the noise associated with the adaptive threshold algorithm and specific floes moving in or out of the box. The standard error associated with this linear fit is less than 0.01 m, so has no perceptible impact on the estimate of characteristic relative velocities. The accuracy of the estimate of radius is also limited by the pixel size, which is ~2 cm in the near-field and 12 cm in the far-field.

The change in areal concentration of sea ice over time, $A(t)$, is calculated from the change in pixel intensity $I(t)$. The video in the Supplementary material shows the original and thresholded images projected on the reconstructed ocean surface over a 45 s burst (at 2 × speed). Here we can see the increase in brightness or pixel intensity as floes converge near the crest of waves. Concentration is calculated from the pixel intensity, rather than the coverage in thresholded images, as the adaptive threshold used adjusts based on the brightness so that the resulting binary images do not well represent changes in concentration over time. However, the thresholded images give a good estimate for the average areal coverage for the entire time series, as can be qualitatively seen in the example in Figure 4. The average areal concentration from binary, thresholded images ($A_{thresholded}$) is used to normalize the pixel intensities, such that the average value produced by both methods is equivalent:

$$A(t) = \frac{\bar{I}(t)}{\langle \bar{I}(t) \rangle / \langle A_{\mathrm{thresholded}} \rangle}. \tag{5}$$

https://doi.org/10.1017/aog.2019.35 Published online by Cambridge University Press

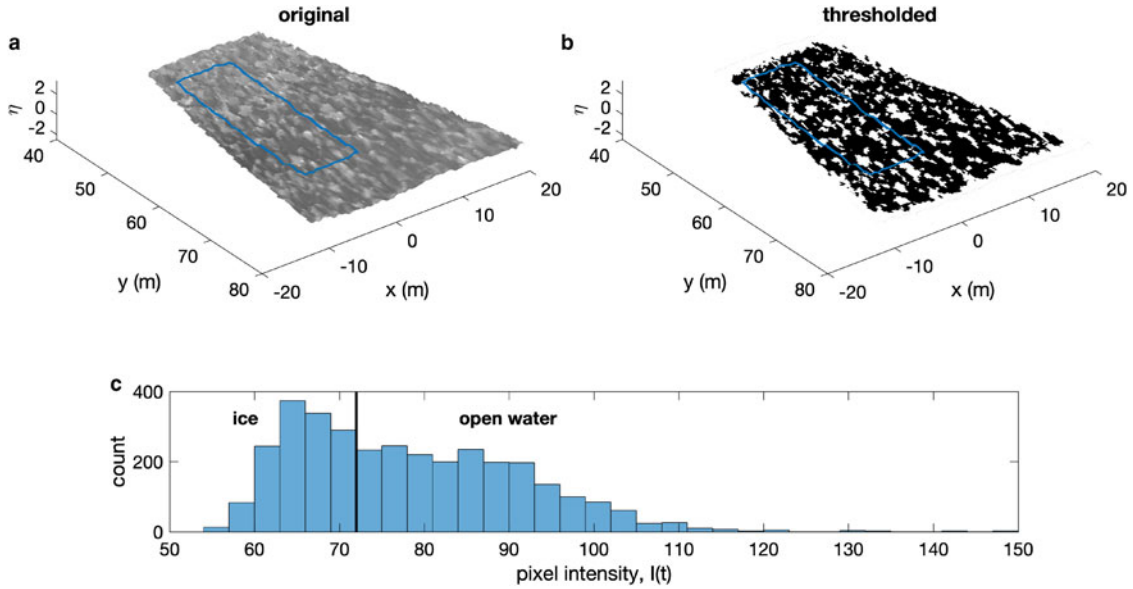


Fig. 4. Example of (a) original and (b) thresholded images from stereo camera on 11 October 2015 21:30, projected onto geographic reference frame. Blue boxes represent the analysis box over which all values in Figure 6 are estimated. (A corresponding video is provided as Supplementary material.) (c) Histogram of pixel intensities from original image. The vertical line represents delineation of ice and open water based on Eqn. (5).

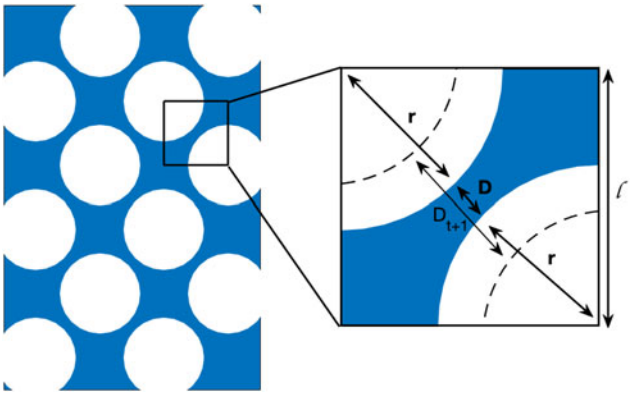


Fig. 5. Schematic demonstrating the calculation of average distance between floes, in Eqn. (4), using the areal concentration and floe radius. This method assumes uniform floe radius and uniform floe spacing. Dotted lines demonstrate the increase in floe distance D as floes diverge at some future time $t+1$.

The distribution of pixel intensity is not clearly bimodal (Fig. 4c), as would be ideal to clearly separate sea ice from open water. The threshold value (shown by the vertical black line) is instead determined as the pixel intensity that is necessary to produce that same average concentration that is estimated by applying an adaptive threshold. An example of the concentration estimated from thresholded images and pixel intensities is shown in Figure 6b. The overline denotes a spatial average, and brackets are used to denote a temporal average.

Time series of average distance between floes (Fig. 6c) are calculated from these estimates of radius and concentration using Eqn. (4). The time series of average distance between floes is linearly de-trended if it is complete (i.e. without any periods of substantial rolling), and smoothed with a span of 5 points (1 s). Time series of relative velocity between floes are then calculated using the change in average distance between floes,

$$\overline{\Delta V_{\mathrm{obs}}}(t) = \left(\frac{\mathrm{d}\overline{D_{\mathrm{obs}}}(t)}{\mathrm{d}t}\right)\frac{1}{2}. \tag{6}$$

The derivative of the distance over time must be divided by two to determine the relative speed of each floe in a pair. In order to avoid artificially introducing a lag, this derivative is done using distances before and after each point in time, i.e. $\overline{\Delta V}(\mathrm{i}) = (D_{\mathrm{i+1}} - D_{\mathrm{i-1}}/t_{\mathrm{i+1}} - t_{\mathrm{i-1}})½$. The result is a characteristic speed of ice floes relative to each other within the domain. In reality, the convergence and divergence will be primarily along the axis of wave propagation. As we are calculating a scalar characteristic or average distance between floes, this will not affect the result. Although this estimate is spatially averaged within the domain, it is phase-resolved in time.

Prediction of ice velocities based on wave slope

Relative motion between floes is expected based on the gradient of orbital velocities along the sloped wave surface, as shown in the schematic in Figure 1. We can estimate this relative motion using the map of surface elevation over the field of view for each frame, produced from the stereo video processing (e.g., Fig. 4). A 2D linear fit is used to estimate the maximum slope ($\mathrm{d}\eta/\mathrm{d}x$) within the processing box in each frame. The spatial average of the relative velocity between floes is then

$$\overline{\Delta V_{\eta}}(t) = \frac{2\pi}{T_{\mathrm{e}}}\frac{\mathrm{d}\eta}{\mathrm{d}x}2\bar{r}. \tag{7}$$

The average diameter of floes ($2\bar{r}$) is used here as an approximate scale over which relative motion is occurring.

Prediction based on Herman model

The average relative velocity of floes predicted by the Herman (2018) model is also calculated using the change in distance between floes. The average distance between floes based on Herman's Eqn. (27) is:

$$D_{\mathrm{H}}(t) = 2r\left(\frac{1-A}{A}\right) - 2\left(\frac{H_{\mathrm{s}}}{2}\right)\sin\left(\frac{kr}{A}\right)\cos\left(\omega t + \frac{kr}{A}\right). \tag{8}$$

This equation assumes initially equally spaced floes with identical radii, and disregards the effect of friction. We use the time-averaged concentration, $\langle\bar{A}\rangle$, such that the time variation is

https://doi.org/10.1017/aog.2019.35 Published online by Cambridge University Press

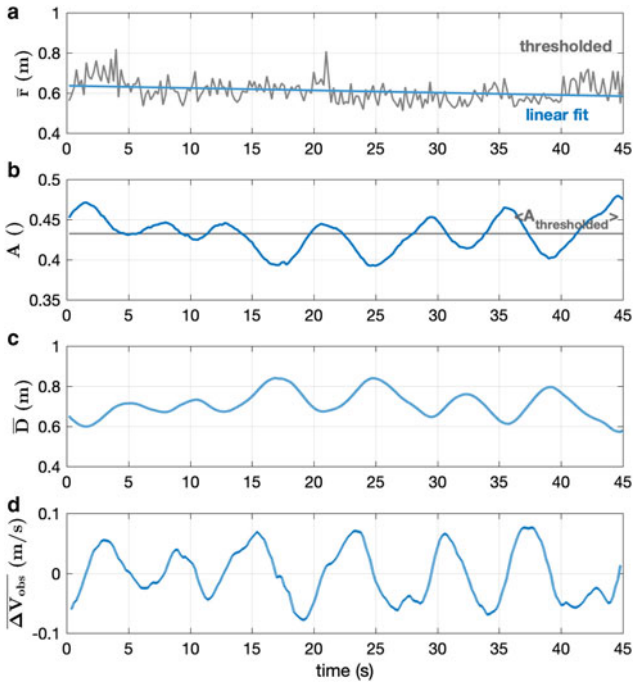


Fig. 6. Example time series of observed floe characteristics, demonstrating methods used to estimate relative velocities. (a) Linear fit (blue line) to average radius in each frame (gray line). (b) Aerial ice coverage determined from image intensity (Fig. 4a), normalized to the average coverage in thresholded images (Fig. 4b; Eqn. (5)). (c) Distance between floes calculated using Eqn. (4). (d) Characteristic relative velocity of floes calculated using Eqn. (6).

primarily a result of the wave motion $\overline{\eta}$ averaged over the box in Figure 4:

$$\overline{D_{\mathrm{H}}}(t) = 2\overline{r}\left(\frac{1-\langle\bar{A}\rangle}{\langle\bar{A}\rangle}\right) - 2\,\overline{\eta}\,\sin\left(\frac{k\overline{r}}{\langle\bar{A}\rangle}\right). \tag{9}$$

Similar to Eqn. (6), the relative velocity between floes predicted by Herman (2018) is the change in average distance between floes over time:

$$\overline{\Delta V_{\mathrm{H}}}(t) = \left(\frac{\mathrm{d}\overline{D_{\mathrm{H}}}(t)}{\mathrm{d}t}\right)\frac{1}{2}. \tag{10}$$

Results

Example phase-resolved velocities

The time series in Figure 7 shows an example of phase-resolved orbital and relative floe velocities using the first 45 s of the observations from 11 October 21:30. The net motion of floes due to orbital velocities (Fig. 7b), calculated from mean surface elevation (Fig. 7a), is approximately an order of magnitude larger than the relative motion of floes (Fig. 7d). As ice floe motion closely follows the wave motion, relative velocities are expected to be small.

The comparison of relative velocities from observations with predictions from the two models in Figure 7d shows that both models are able to describe the magnitude of velocities, as well as the key features of temporal variability. Comparison of the time series predicted by the Herman model and wave slope methods with observations has correlation coefficients of $R^2 = 0.62$ and $R^2 = 0.77$, respectively. We can further see that the Herman model predicts relative velocities well because it is capturing variability in the average distance between floes (Fig. 7c).

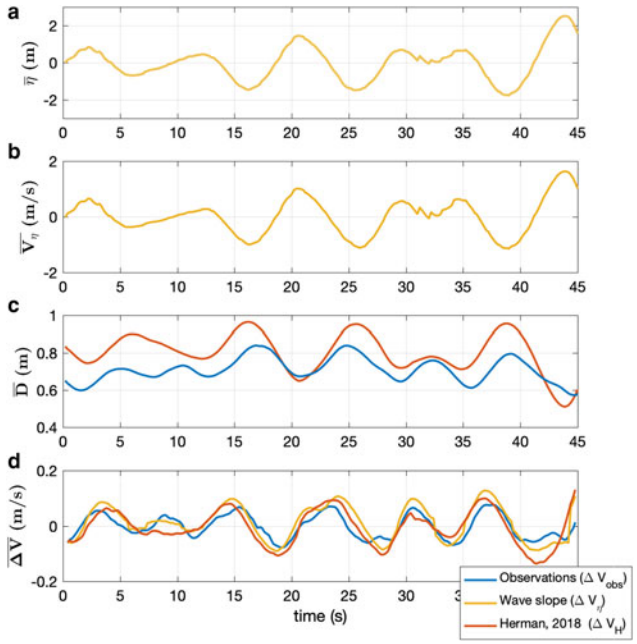


Fig. 7. Example time series of mean and relative velocity estimates for the first 45 s of observations on 11 October 21:30. (a) Mean surface elevation; (b) mean orbital velocity (Eqn. (1)); (c) average distance between floes from observations and Herman model; and (d) relative velocity estimates for the three different methods.

Comparison of relative velocities

Relative velocities were estimated using the three methods described for all five observation periods (Table 1). Figure 8 compares the average relative speed $\langle|\overline{\Delta V}|\rangle$ determined by each method as a function of bulk wave steepness (H_s/L_e). In general, both models replicate the observations well. The bars represent the standard deviation of relative speed, and so are expected to be large based on the variation in velocity at different points in a wave period. We generally observe larger relative velocities of floes with increasing wave steepness. Steeper waves are expected to result in a larger gradient of orbital velocities at the surface. There was no significant phase lag between the observed relative velocities and predictions from the models for any of the observations.

Velocity estimates from observations are expected to have some error based on the assumptions behind Eqn. (4): that floes have uniform shape and radius, and are evenly spaced at all times (Fig. 5). Although typically disc-shaped, pancakes are rarely perfectly circular; pancake sea ice has an average aspect ratio of 1:1.6 (Alberello and others, 2019). The ellipticity of pancakes will affect the absolute values of D_{obs} calculated, but should have minimal effect on relative distance and thus relative velocity if an equivalent radius is used. The calculation of relative distances and velocities are more likely to be affected by assuming that floes are all the same average radius and evenly spaced. Floe size distributions of pancakes do not seem to follow any sort of power law distribution, but do typically have some spread in observed radii (Alberello and others, 2019). Due to the challenge of identifying and tracking individual floes, we are unable to calculate the associated error. These assumptions emphasize that calculated $\overline{V_{\mathrm{obs}}}$ should be treated as a characteristic relative speed, rather than an absolute relative speed. Additionally, the width of the analysis box along the axis of wave propagation is nearly 30% of the wavelength during the shortest wavelength conditions, which may result in an underestimation of relative velocities amplitudes over time.

Velocity estimates from both models are strongly dependent on the choice of defining wave period and the associated wavenumber, as a result of their appearance in Eqns. (7) and (8). The energy-

https://doi.org/10.1017/aog.2019.35 Published online by Cambridge University Press

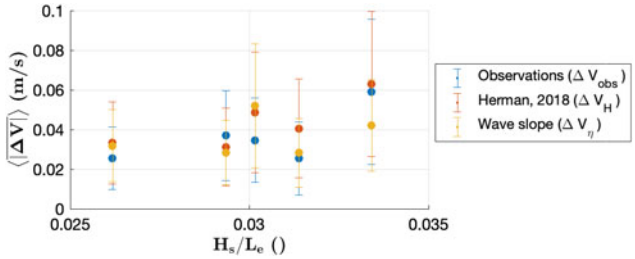


Fig. 8. Average absolute value of relative floe velocities from observations (blue) compared with expectation based on gradient in orbital motion from wave slope (yellow), and Herman model (red), as a function of wave steepness (determined from bulk parameters). Bars represent standard deviation of absolute values of relative velocities.

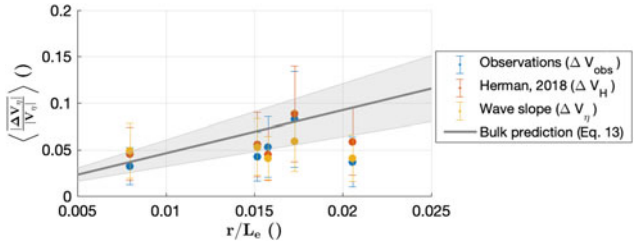


Fig. 9. Average relative floe velocities normalized by orbital velocities as a function of the ratio of average floe radius to bulk wavelength. As in Fig. 8, points represent velocities from observations (blue), expectation based on gradient in orbital motion from wave slope (yellow), and Herman model (red), and bars represent standard deviation of absolute values of relative velocities. The grey line represents expectation based on linear theory, determined by bulk wave parameters (Eqn. (13)), and shading represents the standard deviation of relative velocity resulting from the assumption of monochromatic regular waves.

weighted wave period is used throughout, as it represents the time scale of the variance of motion resulting from the wave field, and is a more statistically robust estimate than the peak wave period. Use of the peak period results in substantially lower estimates of relative velocity for all methods (not shown), as it is an average of 50% larger for the conditions observed. Additionally, we use significant wave height and energy-weighted wave period calculated from the complete 5 min stereo record, which are comparable to wave parameters that may be obtained from other observational methods or models, while the velocities use shorter records. Comparison of significant wave height from the entire record with those from the shorter records (calculated using zero-crossing method) show that they may be as much as 30% different.

Relative velocity estimates from bulk wave and ice parameters

The model estimates in Figure 8 require detailed knowledge of the time evolution of mean surface elevation η, in addition to bulk wave and ice characteristics. As this information is rarely available, we introduce estimates from these models that rely solely on bulk estimates. We propose a method to estimate relative velocities based on bulk parameters by using the definition of $\eta = (H_{\mathrm{rms}}/2)\cos(kx - \omega t)$ to estimate the wave slope

$$\frac{\mathrm{d}\eta}{\mathrm{d}x} = \frac{kH_{\mathrm{s}}}{2\sqrt{2}} \cdot \sin(kx - \omega t). \tag{11}$$

Here, $H_{\mathrm{rms}} = H_{\mathrm{s}}/\sqrt{2}$ has been substituted in so that the more commonly reported significant wave height can be used. To get a characteristic value of relative velocity, comparable to those in Figure 8, we average the absolute value and substitute in $k = 2\pi/L$ to get

$$\left\langle \left| \frac{\mathrm{d}\eta}{\mathrm{d}x} \right| \right\rangle = \frac{\pi H_{\mathrm{s}}}{L_{\mathrm{e}}\sqrt{2}} \cdot \frac{2}{\pi} = \frac{2H_{\mathrm{s}}}{\sqrt{2}L_{\mathrm{e}}}, \tag{12}$$

where $\langle\rangle$ represents a temporal average. Substituting this back into Eqn. (7) gives

$$\langle|\overline{\Delta V_\eta}|\rangle = \frac{8\pi}{\sqrt{2}} \cdot \frac{H_{\mathrm{s}}\overline{r}}{T_{\mathrm{e}}L_{\mathrm{e}}}. \tag{13}$$

As wave orbital velocities are proportional to H_s/T_e (Eqn. (2)), Eqn. (13) can be re-arranged to determine relative floe velocity normalized by mean floe velocity as a function of the ratio of average radius to wavelength. Figure 9 compares the normalized velocity determined from bulk parameters (grey line) with values from observations and both models. The prediction using bulk parameters generally captures the observed patterns, but with values that are an average of 50% higher than observations. The over-prediction may be a result of the drag and added mass of the ice floes, both of which would reduce the relative velocities. In our observations, average floe radius is typically a few percent of the wavelength and relative velocities are around 5-10 percent of wave orbital velocities.

The simple model using bulk parameters predicts that normalized relative velocities should increase with larger values of r/L_e. The observed normalized relative floe velocities follow this pattern, with the main exception being the observation furthest to the right in Fig. 9, which is from the 24 October 22:20 case. This observation coincided with the thickest sea ice. Here, added mass associated with sea ice may be important. However, both models agree well with observations, which indicates that conditions resulting in lower relative velocities are well captured by the time variation of the wave field.

The shaded error bar in Fig. 9 shows the standard deviation in relative speed that would be expected based on the same assumptions behind Eqn. (13). The deviation of observations from the mean (blue bars) are comparable to those predicted. Disparities in both mean and standard deviations of relative velocity observations and bulk predictions may be a result of divergence from monochromatic wave shape, and the smaller spatial and temporal coverage of the domain compared to bulk parameters.

Predictions of relative velocity based on Eqn. (13) are shown in Fig. 10 for a range of wave and ice values that may be expected in sea ice. Across the parameter space, relative velocities are always small ($\mathcal{O}(10^{-1})$). These relative velocities have implications for energy loss associated with collisions and turbulence, as discussed further in the next section. Values are expected to increase as both wave orbital velocities ($\langle|\overline{V_\eta}|\rangle$) and relative floe size (r/L_e) increase.

It should also be noted that observations presented here span a narrow parameter space compared to what might occur in polar oceans. Wave heights range from 0.9–2.5 m, and energy-weighted periods range from 4.3–7.2 s, with all but one observation between 4–5 s (Table 1). Values of $k \cdot r$, which have been proposed to have an inverse relationship with how closely ice follows wave motion (Herman, 2018), are all well below one (i.e. we expect the ice to follow the wave motion quite closely).

We can derive a similar expression for characteristic relative velocities predicted from bulk characteristics using the Herman 2018 model by integrating Eqn. (9).

$$\langle|\overline{\Delta V_H}|\rangle = 2\frac{H_s}{T_e} \cdot \sin\left(\frac{8\pi^2}{g}\frac{\overline{r}}{T_e^2 H_s}\right). \tag{14}$$

This simple model can also be re-arranged to determine relative velocities normalized by orbital velocities (Eqn. (2)) as a function

https://doi.org/10.1017/aog.2019.35 Published online by Cambridge University Press

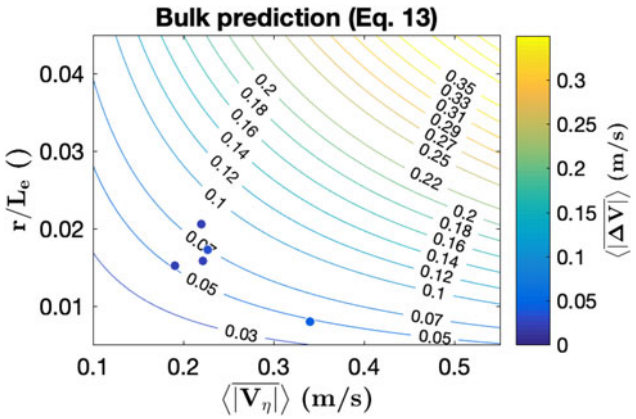


Fig. 10. Contours of average relative floe velocity predicted using linear theory with bulk wave and ice parameters (Eqn. (13)). Filled points show observed values within the parameter space.

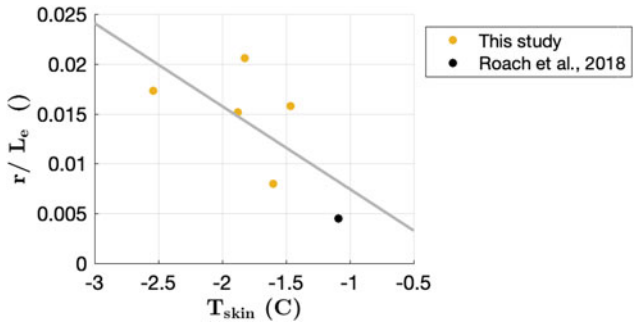


Fig. 11. Average floe radius, scaled by wavelength, as a function of skin temperature. Yellow points are from this study, and black point is from Roach and others (2018).

of bulk wave parameters and average floe radius. Predictions using this equation show similar patterns based on bulk wave parameters as those predicted by Eqn. (13), and so are not shown here. Herman (2018) suggested that floes should more closely follow wave motion as kr approaches zero and that floe motion is less a function of the radius when $2\pi/k > 10r$, as is the case for all observations here (Table 1). In this regime of small floes, observed relative floe motions do not vary significantly from the wave motion. As ice floes become larger, we may expect the Herman (2018) model to become more accurate. However, this has not been tested as we have sparse observations throughout the parameter space (Fig. 10). More observations are needed to determine the validity of these models under such conditions.

Discussion

Implications for pancake growth

It is well understood that the formation of pancakes occurs as a result of wave motion during ice formation conditions, but our ability to predict the growth rate and size of pancake floes is still limited. Shen and others (2001) proposed a theoretical model for growth of pancake ice in a wave field, in which the lateral extent of floes is limited by either tensile or bending stress resulting from the surface wave field. Their theoretical model allows estimation of floe radius based on the tensile stress resulting from the wave field as

$$\bar{r} = \sqrt{\frac{C_2 L_e^2}{\pi^3 H_s g \rho_{ice}}}, \tag{15}$$

where C_2 is tensile mode parameter representing the bonding strength associated with freezing. Roach and others (2018) used simultaneous observations of floe growth and wave conditions from a SWIFT buoy during a pancake formation event to provide the first in situ validation of this model. The radius increased linearly as a function of the tensile failure mode $\sqrt{2L_e^2/H_s}$ (see their Fig. 8), indicating that lateral growth was well captured by the tensile stress model (Eqn. (15)). Based on the fit, the tensile mode parameter was estimated as $C_2 = 0.167$ [N/m^2] for the observed conditions. This value is expected to vary under different conditions, and to be related primarily to the temperature.

We use the observations from the present study to test these formulations for pancake growth. The observations span a range of atmospheric and ocean conditions, suggesting a range of tensile mode parameters. We find that the radius of floes, scaled by the wavelength, is related to the skin temperature T_{skin}, measured here by a floating thermistor (Persson and others, 2018) as shown in Fig. 11. This suggests that the skin temperature is important for lateral growth of floes, and may be used to constrain the tensile mode parameter, C_2. The growth rate may be better constrained by the difference of the skin temperature from the freezing temperature, but we are unable to evaluate this relationship due to the lack of a collocated salinity measurement.

We use the average radii and tensile failure modes based on bulk wave characteristics to calculate the C_2 for each observation (Eqn. (15)). C_2 values ranged from 2.1 to 39 N/m^2. Values from this study and Roach and others (2018) are compared with the skin temperature in Fig. 12. These results show that there is a good negative correlation between T_{skin} and C_2 ($R^2 = 0.46$). A logarithmic fit gives the function

$$\ln(C_2) = -3.2T_{skin} - 2.7. \tag{16}$$

As these observations span a small range of floe sizes, additional observations within the parameter space may improve this relationship or illuminate dependencies on other key variables. Parameterizations of the tensile failure mode may then be used to estimate typical floe sizes as a function of ocean skin temperature and bulk wave parameters by merging with Eqn. (15). Additionally, combining these results with the simple models in Eqns. (13) and (14) may allow estimation of the normalized relative velocity with only ocean skin temperature and wave height.

Implications for wave energy loss

Improving estimates of the rate of wave energy dissipation remains an essential question for progressing understanding of waves in sea ice (Shen, 2019). Wave models in ice-covered areas represent the sink of wave energy attenuated by the ice as S_{ice}. Many possible mechanisms contributing to the total rate of wave energy attenuation have been proposed. Here, we discuss two possible mechanisms related to the relative velocities observed: collisions and turbulence.

The motion of floes with waves can result in collisions of floes, particularly when ice concentrations are high and waves are large. The force associated with floe-floe collisions has been described as a mechanism for wave energy attenuation (Shen and others, 1987). Collisions are also a key component of pancake ice formation and growth (Shen and others, 2001), and the associated energy goes at least in part into lateral floe growth and evolution (such as through welding). Dissipation of wave energy from collisions is expected to scale with the relative kinetic energy of the ice floes. We estimate it here, in a fashion similar to the formulation in Shen and others (1987), by using the square of the observed

https://doi.org/10.1017/aog.2019.35 Published online by Cambridge University Press

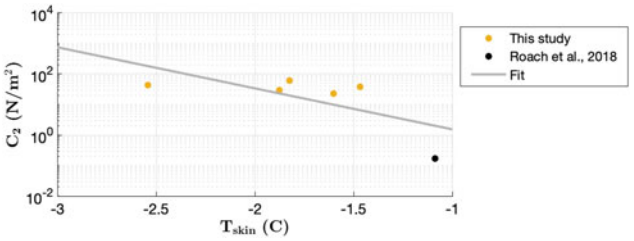


Fig. 12. Tensile mode parameter C_2 as a function of the ocean skin temperature T_{skin}. Yellow points are those determined for this study using Eqn. (15), and black point is from Roach and others (2018). Logarithmic fit to these data (grey line) is given in Eqn. 16.

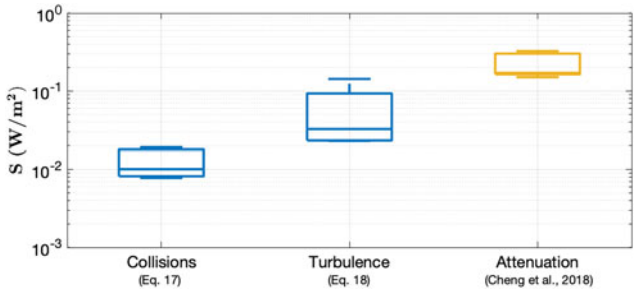


Fig. 13. Boxplot showing total dissipation of wave energy S expected as a result of floe-floe collisions and ice-ocean turbulence generation, compared to the dissipation associated with observed wave energy attenuation between wave buoys (yellow). Each bar shows the average, inter-quartile range, and total range for the five observations.

relative velocities to describe the change in kinetic energy that occurs when ice floes collide a rate of once per wave period T_e:

$$S_{collisions} \approx \frac{\Delta KE}{AT_e} \approx \frac{\frac{1}{2}\rho_{ice} z_{ice} \left\langle |\overline{\Delta V_{obs}}| \right\rangle^2}{T_e}. \quad (17)$$

This represents the maximum kinetic energy that can be harvested by floe-floe collisions, assuming a restitution coefficient of 0 (Shen and others, 1987). Collisions were observed visually during all observation periods, but the assumption that all floes collide once per wave also produces an upper bound on the associated dissipation.

Additionally, the differential velocity of ice relative to the water results in turbulence generation at the ice-ocean interface, which may dissipate wave energy. Kohout and others (2011) made estimates of wave attenuation associated with this process, which showed frequency dependence in agreement with field observations of attenuation. Dissipation of wave energy from turbulence generated by shear between pancakes and the ocean scales with the relative velocity. It is approximated here using observed relative velocities as:

$$S_{turbulence} \approx \rho_w \left\langle |\overline{\Delta V_{obs}}| \right\rangle^3, \quad (18)$$

where ρ_w is the density of the ocean water. This approximation is similar to scalings that are used for law-of-the-wall boundary layers, though such a classic layer is not necessarily expected beneath pancake ice. Here, $\left\langle |\overline{\Delta V_{obs}}| \right\rangle$ is analogous to the friction velocity u^*, or the velocity scale of the energy containing eddies in a turbulent cascade. This is supported by the magnitude of the turbulent velocity fluctuations (also a few cm/s) measured just below the ice using SWIFT buoys (Smith and Thomson, 2019).

We compare total dissipation rates estimated for the two relevant wave energy loss mechanisms ($S_{collisions}$ and $S_{turbulence}$) with those calculated from observed wave attenuation (Fig. 13). Total wave energy dissipation per unit area is estimated based on observed wave attenuation as the change in wave energy between two SWIFT wave buoys (temporally collocated by Cheng and others, 2017) as

$$S_{attenuation} \approx \frac{\mathrm{d}EC_g}{\mathrm{d}x}. \quad (19)$$

Some of the SWIFT deployments used here are up to 3 km away from the stereo video observation area, but are expected to generally capture the same wave attenuation conditions. These observations correspond to average wave attenuation rates ranging from $\alpha = 2 \times 10^{-5}$ to 2×10^{-4}.

The estimates of energy dissipation from ice-ocean turbulence are larger than those from from collisions. Although there can be high kinetic energy loss associated with collisions, they are brief in time compared to the relatively continuous energy loss that can occur via turbulence generation. Additionally, the assumption that all floes collide each wave period with full harvesting of turbulent kinetic energy represents a maximum possible dissipation estimate. As a result, collisions are likely even less important than indicated by this scaling. As both proposed attenuation mechanisms scale with the relative ice velocities, they are expected to increase with wave steepness. This is consistent with results from a recent laboratory experiment which found that attenuation is greater for the same sea ice with a steeper wave field (Toffoli and others, 2015).

Observations from the Sea State experiment in 2015 have resulted in a number of recent studies providing insight into turbulence under pancake and frazil sea ice. Measurements of near-surface turbulent dissipation across a range of wave and sea ice conditions were used to suggest that the production of turbulence underneath thin pancake sea ice largely balances the wind input (Smith and Thomson, 2019). Using the same dataset, Voermans and others (2019) showed that the turbulence underneath the ice can account for nearly all of the observed wave attenuation. Although the mechanisms proposed in these papers may seem contradictory, the results of the present study help us reconcile the results.

We find that the relative velocity of floes, which likely generates turbulence through ice-ocean shear, is a function of the bulk steepness of the waves (Fig. 8). The input of wind energy into the waves will increase (or maintain) wave steepness (e.g., Plant, 1982), even as energy is being attenuated by the sea ice. Smith and Thomson (2019) found that the rate of wind input is suppressed in the ice, but that the wind is still doing work on the surface. Thus, this wind work may maintain wave steepness (which would otherwise decrease rapidly in ice), which in turn drives the relative motion of the pancakes and turbulent eddies of a similar kinematic scale just below the ice. In other words, dissipation (and therefore attenuation) increases with higher wind input because the waves are generating turbulence through relative ice motions. This is in agreement with recent work showing that wind input may contribute a significant portion of the attenuated wave energy, and so is essential to consider in order to accurately predict wave energy (Li and others, 2017).

The sum of wave energy dissipation that is estimated by these relative velocities is still somewhat lower than the dissipation required to explain the observed wave attenuation (Fig. 13). This discrepancy is likely a result of other attenuation mechanisms that have not been considered here. For example, recent work by Rabault and others (2019) suggested that the convergence of frazil may create small-scale eddy structures that dissipate energy via turbulence. This has similar underlying

https://doi.org/10.1017/aog.2019.35 Published online by Cambridge University Press

mechanisms to attenuation from pancake collisions discussed. However, it can occur much more frequently due to the potentially small size and high concentration of frazil, and so could dissipate more energy overall than floe-floe collisions. Overwash was not observed in the measured conditions (see Supplemental Video), but could be another potential mechanism for wave attenuation associated with pancake floe motion.

All of these possible mechanisms are encapsulated in the viscosity and elasticity parameters used in viscous and viscoelastic models for attenuation (e.g., De Carolis and Desiderio, 2002; Wang and Shen, 2010; Sutherland and others, 2019), which are calibrated by fitting the model to observations (Cheng and others, 2017; Doble and others, 2015). However, one major critique of these models is that unrealistically high viscosity values are necessary in order to describe attenuation observations. For the observations used in this study, Cheng and others (2017) calculated viscosity parameters generally between $3.2 - 5.2$ m^2/s, except for a value of 27 m^2/s from the first observation (11 October). The mechanism proposed by Rabault and others (2019) could possibly account for the extremely high viscosity values necessary to reproduce attenuation observations using viscous models, but there has not yet been any work to constrain dissipation via this mechanism. Describing this process is challenging due to the lack of knowledge regarding frazil concentration and distribution in the water column. Determining the dominant attenuation mechanism specific to different wave and ice conditions remains a key requirement, as well as a key challenge, for understanding wave-ice interactions.

Summary

Shipboard stereo video is able to simultaneously resolve wave motion and relative motion of pancake floes. Stereo video captured in the Beaufort Sea in 2015 provides the first in situ observations of relative floe motion in a wave field that are resolved in both space and time.

The relative velocities of floes are captured well by existing models using observations of the surface elevation and slope. Simplifications of these models that utilize bulk parameters predict the general magnitude of relative velocities, but may somewhat over-estimate velocities, especially as sea ice radii increase. Additional observations under different wave forcing and ice conditions are necessary to determine the appropriate correction factors for estimating characteristic relative floe velocity with bulk parameters only.

The relative velocity of floes is relevant for two possible mechanisms that contribute to wave energy loss: floe-floe collisions and turbulence from ice-ocean shear. Estimates of wave energy loss from ice-ocean turbulence exceed those from pancake collisions, and can explain most of the observed wave attenuation. The steepening of waves with wind input in the ice may increase the relative velocities of floes, and thus the attenuation of wave energy through turbulence may be intrinsically related to wind forcing.

Supplementary material

To view supplementary material for this article, please visit https://doi.org/10.1017/aog.2019.35.

Acknowledgments. The observations used in this work were funded by the Office of Naval Research awards N00014-13-1-0284 and N00014-17-1-2544 under the 'Sea State and Boundary Layer Physics of the Emerging Arctic Ocean' DRI, initiated by Scott Harper and Martin Jeffries. Alex de Klerk and Joe Talbert built and supported operation of the stereo camera system. Mike Schwendeman developed the original stereo processing that were adapted for use in this work, and provided support with operation and processing of stereo results. We acknowledge two reviewers whose comments improved the manuscript. Data are available at www.apl.uw.edu/arcticseastate.

References

Alberello A and 6 others (2019) Brief communication: Pancake ice floe size distribution during the winter expansion of the antarctic marginal ice zone. *The Cryosphere*, **13**(1), 41–48.

Benetazzo A, Francesco B, Filippo B, Sandro C and Mauro S (2017) Space-time extreme wind waves: Analysis and prediction of shape and height. *Ocean Modelling*, **113**, 201–216.

Campbell AJ, Bechle AJ and Wu CH (2014) Observations of surface waves interacting with ice using stereo imaging. *Journal of Geophysical Research: Oceans*, **119**(6), 3266–3284.

Cheng S and 10 others (2017) Calibrating a viscoelastic sea ice model for wave propagation in the Arctic fall marginal ice zone. *Journal of Geophysical Research: Oceans*, **122**(11), 8770–8793.

Collins C, Doble M, Lund B and Smith M (2018) Observations of surface wave dispersion in the marginal ice zone. *Journal of Geophysical Research: Oceans*, **123**(5), 3336–3354.

De Carolis G and Desiderio D (2002) Dispersion and attenuation of gravity waves in ice: A two-layer viscous fluid model with experimental data validation. *Physics Letters A*, **305**(6), 399–412.

Doble MJ (2009) Simulating pancake and frazil ice growth in the Weddell Sea: A process model from freezing to consolidation. *Journal of Geophysical Research: Oceans*, **114**(C9), 1–10. doi: 10.1029/2008JC004935

Doble MJ, Coon MD and Wadhams P (2003) Pancake ice formation in the Weddell Sea. *Journal of Geophysical Research: Oceans*, **108**(C7), 1–13. doi: 10.1029/2002JC001373

Doble MJ, De Carolis G, Meylan MH, Bidlot JR and Wadhams P (2015) Relating wave attenuation to pancake ice thickness, using field measurements and model results. *Geophysical Research Letters*, **42**(11), 4473–4481.

Grotmaack R and Meylan MH (2006) Wave forcing of small floating bodies. *Journal of Waterway, Port, Coastal, and Ocean Engineering*, **132**(3), 192–198.

Herman A (2011) Molecular-dynamics simulation of clustering processes in sea-ice floes. *Physical Review E*, **84**(5), 056104.

Herman A (2013) Numerical modeling of force and contact networks in fragmented sea ice. *Annals of Glaciology*, **54**(62), 114–120.

Herman A (2018) Wave-induced surge motion and collisions of sea ice floes: Finite-floe-size effects. *Journal of Geophysical Research: Oceans*, **123**(10), 7472–7494.

Kohout AL, Meylan MH and Plew DR (2011) Wave attenuation in a marginal ice zone due to the bottom roughness of ice floes. *Annals of Glaciology*, **52**(57), 118–122.

Lange M, Ackley S, Wadhams P, Dieckmann G and Eicken H (1989) Development of sea ice in the weddell sea. *Annals of Glaciology*, **12**, 92–96.

Li H, Lubbad R and others (2018) Laboratory study of ice floes collisions under wave action. *The 28th International Ocean and Polar Engineering Conference*, International Society of Offshore and Polar Engineers, Sapporo, Japan.

Li J and 5 others (2017) Rollover of apparent wave attenuation in ice covered seas. *Journal of Geophysical Research: Oceans*, **122**(11), 8557–8566.

Meylan MH, Yiew LJ, Bennetts LG, French BJ and Thomas GA (2015) Surge motion of an ice floe in waves: comparison of a theoretical and an experimental model. *Annals of Glaciology*, **56**(69), 155–159.

Niioka T and Kohei C (2010) Sea ice thickness measurement from an ice breaker using a stereo imaging system consisted of a pairs of high definition video cameras. *International Archives of the Photogrammetry, Remote Sensing and Spatial Information Science, Kyoto Japan*, **38**(8), 1053–1056.

Persson POG and and 8 others (2018) Shipboard observations of the meteorology and near-surface environment during autumn freeze-up in the Beaufort/Chukchi Seas. *Journal of Geophysical Research: Oceans*, **123**(7), 4930–4969.

Plant WJ (1982) A relationship between wind stress and wave slope. *Journal of Geophysical Research: Oceans*, **87**(C3), 1961–1967.

Rabault J, Sutherland G, Jensen A, Christensen KH and Marchenko A (2019) Experiments on wave propagation in grease ice: Combined wave gauges and particle image velocimetry measurements. *Journal of Fluid Mechanics*, **864**, 876–898.

Roach LA, Smith MM and Dean SM (2018) Quantifying growth of pancake sea ice floes using images from drifting buoys. *Journal of Geophysical Research: Oceans*, **123**(4), 2851–2866.

Rohith M, Somanath G, Kambhamettu C and Geiger CA (2009) Stereo analysis of low textured regions with application towards sea-ice reconstruction. *IPCV*, Las Vegas, Nevada, USA, pp. 23–29.

Rottier PJ (1992) Floe pair interaction event rates in the marginal ice zone. *Journal of Geophysical Research: Oceans*, **97**(C6), 9391–9400. doi: 10.1029/92JC00152

Rumer RR, Crissman RD and Wake A (1979) *Ice Transport in Great Lakes*. Great Lakes Environmental Research Laboratory, National Oceanic and Atmospheric Administration, US Dept. of Commerce.

Schwendeman M and Thomson J (2015) A horizon-tracking method for shipboard video stabilization and rectification. *Journal of Atmospheric and Oceanic Technology*, **32**(1), 164–176.

Schwendeman MS and Thomson J (2017) Sharp-crested breaking surface waves observed from a ship-based stereo video system. *Journal of Physical Oceanography*, **47**(4), 775–792.

Shen HH (2019) Modelling ocean waves in ice-covered seas. *Applied Ocean Research*, **83**, 30–36.

Shen HH and Ackley SFA (1991) A one-dimensional model for wave-induced ice-floe collisions. *Annals of Glaciology*, **15**(1), 87–95.

Shen HH and Squire VA (1998) Wave damping in compact pancake ice fields due to interactions between pancakes. *Antarctic Sea Ice: Physical Processes, Interactions, and Variability*, **74**, 325–341.

Shen HH, Hibler WD and Leppäranta M (1987) The role of floe collisions in sea ice rheology. *Journal of Geophysical Research: Oceans*, **92**(C7), 7085–7096. doi: 10.1029/JC092iC07p07085

Shen HH, Ackley SF and Hopkins MA (2001) A conceptual model for pancake-ice formation in a wave field. *Annals of Glaciology*, **33**(2), 361–367, doi: 10.3189/172756401781818239

Smith M and Thomson J (2019) Ocean surface turbulence in newly formed marginal ice zones. *Journal of Geophysical Research: Oceans*, **124**(3), 1382–1398.

Smith M and and 8 others (2018) Episodic reversal of autumn ice advance caused by release of ocean heat in the beaufort sea. *Journal of Geophysical Research: Oceans*, **123**(5), 3164–3185. doi: 10.1002/2018JC013764

Squire VA (2019) Ocean wave interactions with sea ice: A 2019 reappraisal. *Annual Review of Fluid Mechanics*, **AA**, 1–25.

Sutherland G, Rabault J, Christensen KH and Jensen A (2019) A two layer model for wave dissipation in sea ice. *Applied Ocean Research*, **88**, 111–118.

Thomson J (2012) Wave breaking dissipation observed with SWIFT drifters. *Journal of Atmospheric and Oceanic Technology*, **29**, 1866–1882. doi: 10.1175/JTECH-D-12-00018.1

Thomson J and and 28 others (2018) Overview of the Arctic Sea State and Boundary Layer Physics Program. *Journal of Geophysical Research: Oceans*, 8674–8687. doi: 10.1002/2018JC013766

Toffoli A and 6 others (2015) Sea ice floes dissipate the energy of steep ocean waves. *Geophysical Research Letters*, **42**(20), 8547–8554.

Treshnikov AF (1967) The ice of the southern ocean. *Pacific Antarctic Sci., 11th Pacific Science Congress*, Tokyo, Japan. pp. 113–123.

Voermans JJ, Babanin AV, Thomson J, Smith MM and Shen HH (2019) Wave attenuation by sea ice turbulence. *Geophysical Research Letters*, **46**, 6796–6803.

Wang R and Shen HH (2010) Gravity waves propagating into an ice-covered ocean: A viscoelastic model. *Journal of Geophysical Research: Oceans*, **115** (C6), 1–12.

Yiew L, Bennetts L, Meylan M, French B and Thomas G (2016) Hydrodynamic responses of a thin floating disk to regular waves. *Ocean Modelling*, **97**, 52–64.

Yiew LJ, Bennetts L, Meylan M, Thomas G and French B (2017) Wave-induced collisions of thin floating disks. *Physics of Fluids*, **29**(12), 127102.

https://doi.org/10.1017/aog.2019.35 Published online by Cambridge University Press